

Decelerated molecular beams for high-resolution spectroscopy

The hyperfine structure of $^{15}\text{ND}_3$

J. van Veldhoven^{1,2}, J. Küpper¹, H.L. Bethlem^{1,2}, B. Sartakov³, A.J.A. van Roij⁴, and G. Meijer^{1,a}

¹ Fritz-Haber-Institut der Max-Planck-Gesellschaft, Faradayweg 4-6, 14195 Berlin, Germany

² FOM-Institute for Plasmaphysics “Rijnhuizen”, Edisonbaan 14, 3439 MN Nieuwegein, The Netherlands

³ General Physics Institute RAS, Vavilov str. 38, 119991 Moscow, Russia

⁴ Department of Molecular and Laser Physics, University of Nijmegen, Toernooiveld 1, 6525 ED Nijmegen, The Netherlands

Received 25 June 2004 / Received in final form 7 September 2004

Published online 23 November 2004 – © EDP Sciences, Società Italiana di Fisica, Springer-Verlag 2004

Abstract. Ultimately, the resolution of any spectroscopic experiment is limited by the interaction time between the particles that are to be examined and the measuring device. The obtainable spectroscopic resolution in a molecular beam experiment can be considerably improved using samples of slow molecules, as produced, for example, in a Stark-decelerator. This is demonstrated here by measuring the inversion tunneling spectrum of $^{15}\text{ND}_3$ using a pulsed molecular beam that has been decelerated to about 52 m/s. Hyperfine resolved inversion transitions in $^{15}\text{ND}_3$ in the $|J, K\rangle = |1, 1\rangle$ state (around 1.43 GHz) are induced in a microwave region, and $^{15}\text{ND}_3$ molecules that have undergone the transition are subsequently detected using a UV-laser based ionization detection scheme. To increase the signal intensity, the decelerated molecular beam is both transversally and longitudinally focused into the laser detection region. The observed spectral width of individual hyperfine transitions in the fully resolved spectrum is about 1 kHz, and the standard deviation of the best fit is 62 Hz.

PACS. 33.15.Pw Fine and hyperfine structure – 33.20.Bx Radio-frequency and microwave spectra – 33.40.+f Multiple resonances – 33.70.Jg Line and band widths, shapes, and shifts – 39.10.+j Atomic and molecular beam sources and techniques

1 Introduction

Since frequencies can be measured with by far the highest accuracy ($\sim 10^{-15}$), testing of fundamental theories in physics often relies on spectroscopy. Examples of this include the highly accurate measurements of the Rydberg constant and of the $1S$ Lamb shift [1–4]. To detect parity violation effects induced by weak interactions in chiral molecules, accurate measurements of transition frequencies in enantiomers are performed [5–8]. Promising systems for that are the fluorohalogenomethanes [6] and the most accurate experiments so far, at the 10^{-13} level for the relative transition frequency difference between enantiomers, have been performed on molecules from this class [9]. When this experimental accuracy is compared to the theoretically predicted difference it is clear that significant experimental improvements have yet to be made. However, if such experiments were to be performed on the most suitable systems in the collision free environment of a molecular beam, the required accuracy would be within reach [6].

High precision spectroscopic measurements are also undertaken to determine whether there is any time-variation of the fundamental constants [10,11]. Recent astrophysical data [12] suggest that the fine structure constant α has changed by 1 part in 10^5 over the age of the universe, corresponding to a change of 10^{-15} /year if one assumes a cosmological model with linear expansion. If confirmed, this will give very valuable insights into theories that go beyond the Standard Model. Therefore, there is a large interest in independent tests of these results [13,14]. Various laboratory tests are being performed using clocks based on atomic transitions. These tests are mainly sensitive to the time-variation of α . Simultaneously, high-resolution spectroscopic measurements on molecules are performed, which can constrain the bound of the time-variation of the ratio of the electron-to-proton mass [15,16]. Other molecular spectroscopic experiments that are currently being performed as sensitive tests of fundamental symmetries include measurements of the time-reversal-symmetry violating electric dipole moment of the electron (EDM), using YbF [17] and PbO [18], and on the possible parity violating nuclear anapole moments and Z^0 couplings to the nuclear spin [19].

^a e-mail: meijer@fhi-berlin.mpg.de

To improve the laboratory tests of these fundamental concepts it is necessary to further improve the spectral resolution. Ultimately, the achievable resolution in any spectroscopic experiment is limited by the interaction time of the particle that is being investigated with the radiation field, due to the limited size of the interaction region in combination with the non-zero velocity of the examined particles. Obviously, the only two ways to increase the interaction time are to either increase the size of the interaction region or to decelerate, or even trap, the particles. The former has been most successfully implemented in Ramsey-type experiments [20]. The obtainable resolution in these experiments is practically only limited by the requirements on the divergence of the (molecular) beams. In the case of atoms, samples of trapped atoms, either confined “mechanically” [20] or by electro-magnetic fields [21], as well as atomic fountains [22,23], have been used for high-resolution spectroscopy. The use of actively decelerated beams of molecules for high-resolution spectroscopy, as presented in this work, has not been reported yet. It should be mentioned, however, that high-resolution spectroscopic experiments on slow molecules have been performed in the past, for instance by selectively probing the slowest sub-set of molecules in a thermal gas-phase sample using Doppler-free two-photon spectroscopy [24,25].

In this paper we present the application of Stark-decelerated beams in high-resolution spectroscopy, with the particular aim to unravel the hyperfine structure of $^{15}\text{ND}_3$. Over the last years, our group has developed the Stark-deceleration technique and we have used it to produce cold samples of slow polar molecules [26]. The versatility of the Stark-deceleration technique and the relatively large densities of quantum state selected slow molecules obtainable with this method, makes it a prime method for the preparation of molecular samples for precision spectroscopy; experiments are currently underway to use Stark-decelerated beams of ground-state YbF molecules for sensitive EDM measurements [27]. Other promising methods to produce slow molecules for precision spectroscopy have been demonstrated as well. Binding cold atoms together, either with the help of a photon [28] or by using a Feshbach resonance [29], has proven to be an efficient method to make cold molecules. Buffer-gas cooling has been used to cool CaH to 400 mK, and to subsequently trap this paramagnetic radical in an inhomogeneous magnetic field [30,31]; experiments have been proposed to use buffer-gas cooled samples of PbO for sensitive EDM measurements as well [32]. Other methods to produce beams of slow molecules include the selection of the slowest molecules from an effusive thermal beam [33], mechanical slowing using back-spinning nozzles [34,35], and billiard-like inelastic collisions in crossed molecular beams [36].

Ammonia was the first molecule to be observed with microwave spectroscopy [37] and is arguably the most extensively studied system in molecular spectroscopy [38]. Especially the hyperfine structure of $^{14}\text{NH}_3$ has been studied in great detail, most precisely in an ammonia maser [39]. The inversion doubling of $^{14}\text{NH}_3$ is often being used as a textbook example of an accurately known molec-

ular spectrum. The inversion spectra of the deuterated isotopomers, on the other hand, have received considerably less attention [40–42]. In previous work we have presented the inversion spectrum of $^{14}\text{ND}_3$ and $^{15}\text{ND}_3$ as recorded in a molecular beam with a mean velocity of 280 m/s, with a transit-time broadening limited linewidth of 10 kHz [42]. Although those experiments were already performed in a molecular beam that is as slow as possible using “conventional” means, i.e., using the heaviest rare gas carrier and a cooled pulsed beam source, the hyperfine structure could not be completely resolved. Obviously, a better resolution could have been obtained if a longer microwave interaction region, or a set of microwave regions in a Ramsey-type setup, would have been used. In the work presented here, we use a beam of $^{15}\text{ND}_3$ that is decelerated to about 52 m/s. For maximum beam intensity in the laser detection region, transverse focusing and spatial re-bunching (longitudinal focusing) of the decelerated beam is applied. In contrast to the bunching scheme reported previously [43], here we have not used a specifically designed separate buncher, but rather achieve bunching with the help of the last stages of the Stark decelerator. Together, these improvements have enabled us to completely resolve the hyperfine structure and to determine the energies of all individual hyperfine levels of $^{15}\text{ND}_3$ in its $|J, K\rangle = |1, 1\rangle$ state to an absolute accuracy of better than 100 Hz.

2 Experimental

The experiments are performed in a differentially pumped pulsed molecular beam setup, operated at a 10 Hz repetition frequency, depicted in Figure 1. In the source chamber a mixture of typically 5% $^{14}\text{ND}_3$ or $^{15}\text{ND}_3$ in Xe is expanded from 2 bar into vacuum through a pulsed valve (modified General Valve, Series 9) with a 0.8 mm diameter orifice, creating a ~ 100 μs -duration gas pulse. The source chamber is pumped by a 500 l/s turbo-molecular pump (Balzer TPU 500) backed by a rotary pump (Alcatel 2033) and the resulting operating pressure is typically 2×10^{-6} mbar. The nozzle is cooled to -70 °C, resulting in a beam with a mean velocity of about 280 m/s. In the molecular beam all para-ammonia molecules, i.e., about 60% of all $^{14}\text{ND}_3$ molecules, reside in the $|J, K\rangle = |1, 1\rangle$ inversion doublet, the ground state of para-ammonia. Further internal relaxation would require nuclear-spin conversion which does not occur on the timescale of the expansion.

Some 35 mm downstream from the nozzle a 1.5 mm diameter skimmer separates the source chamber from the deceleration chamber. This second chamber is also pumped by a 500 l/s turbo-molecular pump (Balzer TPU 500) and is backed by the same rotary pump as the source chamber, resulting in an operating pressure of 5×10^{-8} mbar. After another 35 mm the beam passes through a 60 mm long hexapole consisting of six 3 mm-diameter rods placed equidistantly on the outside of a circle with a radius of 3 mm. Three alternating rods of this hexapole can be switched to high voltage, typically 10 kV, while the other set of three rods is connected to ground. The hexapole acts as a positive lens for ammonia molecules in

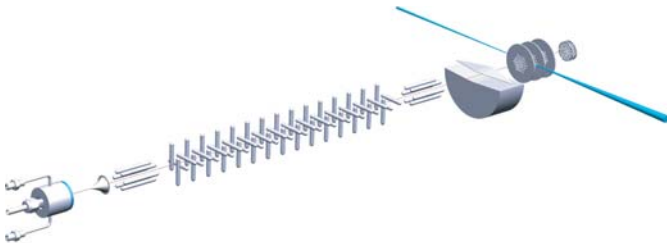


Fig. 1. Experimental set-up. The set-up consists, from left to right, of a pulsed valve to produce a supersonic jet, a skimmer, a hexapole, the Stark-decelerator, another hexapole, the microwave zone, and a laser-ionization/TOF-detector. The whole setup is mounted in a differentially pumped vacuum system.

the low-field seeking hyperfine components in the upper level of the inversion doublet of the $|J, K\rangle = |1, 1\rangle$ state. It is interesting to note that electrostatic focusing of a molecular beam has already been demonstrated over fifty years ago in the original experiments on the ammonia maser [44, 45].

After exiting the hexapole, the molecules enter the decelerator; the first set of electrodes of the decelerator are positioned about 14 mm behind the hexapole. The decelerator used in these experiments consists of 95 sets of parallel electrodes, with a separation of 2 mm between the two electrodes in each set. Each electrode has a diameter of 3 mm and is mounted in the plane perpendicular to the beam axis. The shortest distance between electrodes in adjacent sets is 2.5 mm and each set is rotated over 90° about the beam axis with respect to its neighbors. Within each set one electrode is switched to +10 kV, while the other one is switched to -10 kV. A detailed description of the Stark decelerator in general [26, 46, 47], and of Stark deceleration of a pulsed molecular beam of ammonia in particular [48], was given elsewhere.

In most deceleration experiments that we have performed thus far, the entire length of the decelerator is used to slow a package of state-selected molecules from the initial velocity, normally the mean velocity of the incoming beam, to the desired final velocity. To increase the peak density in the detection region, we use the last stages of the decelerator for spatial re-bunching, or longitudinal spatial focusing, instead. Thus, (part of) the pulsed ammonia beam is decelerated from 280 m/s to 52 m/s using only the first 86 stages of the decelerator. Subsequently, the bunch is allowed to stretch along the molecular beam axis during a free-flight distance of 39.5 mm (7 stages) inside the decelerator; during free flight only a bias voltage of 300 V is applied to the positive electrodes, to prevent Majorana transitions. In the last stage of the decelerator the decelerated package is then re-bunched to obtain a longitudinal spatial focus in the detection region. This type of re-bunching is very similar to the bunching reported by our group before [43], with the only important difference that in the present experiments not a separate, dedicated buncher is used but that the last stage of the decelerator is used for this instead. Since the sets of electrodes in the decelerator are hardwired together we use the same field-strength in the bunching section as in the

deceleration stages. To nevertheless obtain the appropriate longitudinal focusing strength, the time during which the bunching section is on is varied, rather than the electric field strength, as was done before [43].

For transverse focusing of the decelerated molecular beam in the detection region, a second hexapole is mounted 10 mm downstream of the decelerator. This hexapole consists of six 4 mm-diameter, 30 mm long rods mounted on the outside of a circle with a radius of 4 mm. Here, alternating rods are switched to +10 kV and -10 kV. This hexapole is mechanically larger to accept more molecules from the decelerator. The use of both polarity high voltages allows to completely focus the decelerated beam even when the hexapole is only on for 40 μ s, corresponding to an effective thickness of the lens as experienced by the decelerated molecules of only 2 mm. By varying the time at which this hexapole is switched on and off, the position of this thin last focusing lens can be effectively moved along the molecular beam axis over almost the complete length of the hexapole.

In both hexapoles as well as in the decelerator, molecules with a positive Stark-effect, which reside in the upper component of the inversion doublet (in $MK = -1$ states), so-called low-field seekers, are transversally focused, whereas molecules in states with a negative Stark-effect, which reside in the lower component of the inversion doublet (in $MK = 1$ states), so-called high-field seekers, are defocused. Molecules in states with $MK = 0$ (unshifted levels) have a small Stark shift and are not affected much by the electric fields. As a result, almost exclusively ammonia molecules that reside in low-field-seeking hyperfine states of the $|J, K\rangle = |1, 1\rangle$ inversion doublet exit the decelerator, and almost complete population inversion exists in the produced decelerated beam upon entering the microwave zone. The 100 mm long microwave zone, placed 10 mm behind the second hexapole, provides a nearly rectangular field strength distribution along the molecular beam axis with a width (FWHM) of about 65 mm. A cw signal generator (Rohde & Schwarz SMR20) is used to generate the radiation that is needed to induce the inversion tunneling transition of $^{15}\text{ND}_3$ at 1.43 GHz. The synthesizer has a resolution of 0.1 Hz and a quoted stability of 10^{-6} /year. The absolute frequency of the signal generator is tested against the 10 MHz signal of a DCF77 receiver several times during the measurement period by means of a frequency counter (Auerswald FZ-1310) and is found to be better than 10^{-8} , the accuracy of the counter. For 0 dBm incoupling power the field strength on the molecular beam axis is 20 V/m. The experiments are typically performed at power-settings of -30 dBm (0.6 V/m) to -20 dBm (2 V/m) on the microwave synthesizer. Losses due to cabling and connectors are around 1 dBm.

About 50 mm downstream from the exit of the microwave zone molecules are detected using laser-ionization and ion-detection in a home-built time-of-flight mass spectrometer. A frequency-doubled Nd:YAG laser (40% power of a Spectra-Physics Quanta-Ray Pro 230-10) is used to pump a dye laser (Radiant NarrowScan) operating with

DCM. The output of the dye laser is frequency-doubled in a KDP crystal, resulting in typical energies of 15 mJ/pulse at 317 nm with a linewidth of 0.05 cm^{-1} . The tunable UV light is focused into the detection region using a 500 mm focal length lens. The laser beam crosses the molecular beam perpendicularly, and the photoions are extracted coaxially with respect to the molecular beam. The UV-laser based resonance-enhanced 2 + 1 multi-photon ionization (REMPI) scheme enables state-selective detection of the $^{15}\text{ND}_3$ molecules [49]. In the microwave experiments, the UV-laser frequency is kept constant while the microwave frequency is scanned. If the UV-laser is tuned to ionize molecules in the upper component of the inversion doublet, a resonance of the microwave radiation will result in a decrease in ion signal; if the laser is tuned to ionize molecules in the lower component of the inversion doublet, a resonance of the microwave radiation will result in an increase in ion signal. The latter detection scheme has the advantage that it is (almost) background free, and it is the detection scheme that is used for measuring the microwave spectra reported here.

3 Results and discussion

3.1 Deceleration and bunching

In Figure 2 time-of-flight profiles of $^{14}\text{ND}_3$ are shown as obtained using the set-up described above without the microwave zone, i.e., with the laser detection region directly behind the second hexapole. Trace (a) shows a time-of-flight profile of $^{14}\text{ND}_3$ obtained without any electric fields. The measurement shows a broad distribution around a mean arrival time of 2.3 ms, corresponding to an average forward velocity of 280 m/s. The full width at half maximum (FWHM) of the velocity distribution is seen to be around 60 m/s, corresponding to a translational temperature of about 1.6 K in the moving frame of the molecular beam. With the electric fields in the decelerator and hexapoles switched such as to decelerate the central part of the original beam from 280 m/s to about 46 m/s, the time-of-flight distribution shown in trace (b) is obtained. In this case, all stages of the decelerator are used for actual deceleration, i.e., a constant phase-angle, of $\phi = 53^\circ$, is used for deceleration throughout the decelerator, and in each of the 94 stages of the decelerator about 0.68 cm^{-1} of kinetic energy is removed from the accepted bunch of ammonia molecules. Due to the residual velocity spread of the package leaving the decelerator the arrival time distribution of the package in the detection region is relatively broad. A one-dimensional simulation of the time-of-flight profile of this measurement is given in trace (c). One can also see the bunch captured one stable bucket ahead, e.g. 11 mm ahead, of the package containing the synchronous molecule. The relatively long opening time of the pulsed valve ($100 \mu\text{s}$) results in a package of molecules at the entrance of the decelerator with a length of several centimeters. Therefore, some molecules from the original beam are already two stages (one period) ahead inside the decelerator at the time

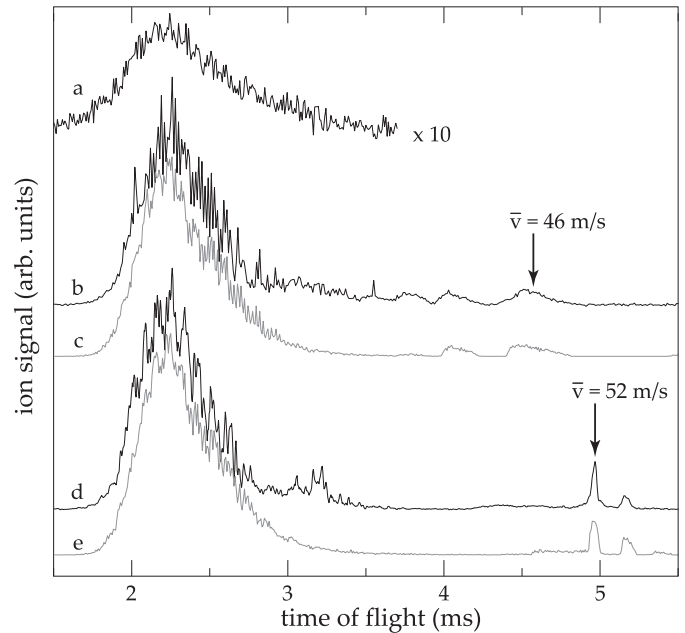


Fig. 2. Observed and calculated time-of-flight distributions of ammonia; the different traces have been given an offset for clarity. Curve (a) is a measurement of the original molecular beam without electric fields. Curve (b) gives a time-profile for a deceleration experiment using all stages for deceleration while curve (c) shows the results of the corresponding trajectory simulation. Curve (d) gives a time-profile for a deceleration experiment with longitudinal spatial focusing of the beam in the detection zone, curve (e) shows the results of the corresponding trajectory simulation.

when the burst sequence for the synchronous molecules starts. When those molecules are then also in the right velocity interval around 280 m/s they are also captured by the electric fields and they are (phase-stable) transported through the decelerator while staying two stages ahead. Consequently, they leave the decelerator earlier, and they do not experience the last two switching processes, since they are then already outside the electrode array. Overall, this package of molecules is 11 mm ahead of the synchronous package and it is traveling at a higher final velocity (around 61 m/s, instead of 46 m/s), and therefore it arrives in the detection region correspondingly earlier. Similarly, there is also a package traveling 11 mm behind the main bunch. Molecules in this package were still in front of the decelerator when the burst sequence started, and they only entered the decelerator when the main bunch was already two stages (one period) further. In order to be captured by the decelerator these molecules must have an initial velocity that is slightly slower, around 277 m/s, since by the time these molecules enter the decelerator the electric fields have already been switched twice for the main bunch. If one stops switching the fields in the decelerator when the main bunch exits, the package trailing by 11 mm is decelerated to the same final velocity as the main bunch and is detected at a time delay after the main bunch directly reflecting the 11 mm spatial

lag. If one continues switching the fields after the main bunch has already exited the decelerator, as is done for the experiments shown in Figure 2b, the package lagging behind is decelerated further, resulting in it being so slow and with such a wide arrival-time distribution that it is not observed at all. In addition, the second hexapole is switched such as to selectively transversally focus only the main bunch.

To further increase the peak density of the slow molecules in the detection region one can perform re-bunching, or longitudinal spatial focusing, of the decelerated bunch [43]. In the experiments performed here the last stage of the decelerator is used as a buncher. For this, a time sequence is applied such as to decelerate the main bunch from 280 m/s down to 52 m/s using only the first 86 stages of the decelerator. This means that the first 86 stages of the decelerator are operated at a constant (higher) phase-angle of $\phi = 58^\circ$, removing 0.74 cm^{-1} kinetic energy from the ammonia molecules per stage. After this, the decelerated package is allowed to longitudinally stretch in free flight in the next 7 stages. The last stage of the decelerator is then switched on for a time-duration of $50 \mu\text{s}$, to obtain a longitudinal spatial focus in the laser detection region. This last stage of the decelerator is switched such as to leave the velocity of the synchronous molecules unchanged, i.e., at phase-angle $\phi = 0^\circ$. The total free flight distance in the decelerator is then 39.5 mm, and during this free flight only a very weak electric field is present inside the decelerator to prevent Majorana transitions. The observed time-of-flight distribution for the decelerated and bunched ammonia molecules is shown in Figure 2, in trace (d). The corresponding trajectory simulation is shown directly underneath, in trace (e). It is seen that, although effectively less molecules are captured in the decelerator in this combined deceleration and bunching scheme due to the necessarily higher phase angle for deceleration and although there are some additional losses during free flight between deceleration and re-bunching due to the velocity spread and due to the absence of transverse focusing, the peak-intensity of the main bunch in the detection region is more than two times larger than in the normal deceleration experiment, e.g., than without re-bunching. As the microwave-UV double-resonance experiments reported here are performed at a fixed timing of the UV-laser, the experiments are sensitive to the peak-intensity and not to the time-integrated intensity, and this increase by a factor two in peak-intensity is very favorable. Also in this combined deceleration and bunching scheme, there are decelerated packages on either side of the main bunch. The package running ahead is hardly visible because it is not re-bunched, as it had already left the decelerator at the time that the buncher was switched on. Due to its long free flight distance this package becomes spread out considerably and is barely recognizable due to its very broad arrival time distribution. The package running 11 mm behind is re-bunched analogously to the main package and this results in a spatial focus 11 mm before the laser detection region. After this focus the package of molecules starts to spread out again and in the detection

region its arrival time distribution is already significantly wider, resulting in a reduced peak intensity.

In all the microwave-UV double resonance experiments reported here a time-sequence equivalent to the one used in trace (d) of Figure 2 is employed. Laser ionization is performed at the peak of the arrival time distribution of the main bunch, thus always detecting ammonia molecules with a velocity of $52 \pm 3.5 \text{ m/s}$.

3.2 Microwave inversion spectrum

To demonstrate the transit-time limitation of the spectral resolution in the beam measurements of the microwave inversion spectrum of $^{15}\text{ND}_3$, a sparse section of the spectrum is recorded for molecular beams with different velocities. In Figure 3 the highest-frequency part of the microwave spectrum is shown for three different velocities. In the measured frequency range there are two transitions with considerable transition strength and one therefore expects a doublet of lines. The upper trace in Figure 3 is measured at 280 m/s, which is, as mentioned earlier, a molecular beam that is already as slow as possible using “conventional” means. The measurement is performed at sufficiently low microwave power (-25 dBm , 1 V/m) to avoid power-broadening. Only a single broad line with a spectral width of 8.7 kHz (FWHM) is observed. In the middle trace the same measurement (-30 dBm , 0.6 V/m) is performed for an ammonia beam that is decelerated to 100 m/s, resulting in a considerably decreased spectral width of approximately 2 kHz . The lowest trace then is the measurement (-30 dBm , 0.6 V/m) for a beam with a mean velocity of 52 m/s, resulting in two base-line separated lines with a width of 1.3 and 1.0 kHz, respectively. These linewidths are deduced from fitting a Lorentzian lineshape to the data, as is shown in Figure 3. In the case of a rectangular microwave field with a width of 65 mm a $(\sin(x)/x)^2$ lineshape with a width (FWHM) of 710 Hz is expected due to transit-time broadening [50]. Deviations from a rectangular field in combination with residual power broadening lead to the observed lineprofiles. It is under these conditions, under which the hyperfine structure can be fully resolved, that the whole inversion spectrum of $^{15}\text{ND}_3$ in the $|J, K\rangle = |1, 1\rangle$ state is measured.

In Figure 4 the pure inversion spectrum of $^{15}\text{ND}_3$ in its $|J, K\rangle = |1, 1\rangle$ state is shown for different velocities and for different microwave powers. The spectra shown in traces (b) and (c) are obtained in steps of 100 Hz in the microwave frequency. At each step, the microwave frequency is paused to record the ion signal, which is determined as the average of 200 ion-count measurements obtained at the pulse rate of 10 Hz of the ionization laser. The spectra shown in traces (b) and (c) of Figure 3 are measured under the same conditions. Trace (a) shows the microwave spectrum as measured in a molecular beam with a mean velocity of 280 m/s, using -20 dBm (2 V/m) of microwave power. The linewidth is about 10 kHz, only slightly better than in the spectra we have reported previously [42]. Although the sub-structure due to the hyperfine splitting can clearly be recognized in this spectrum

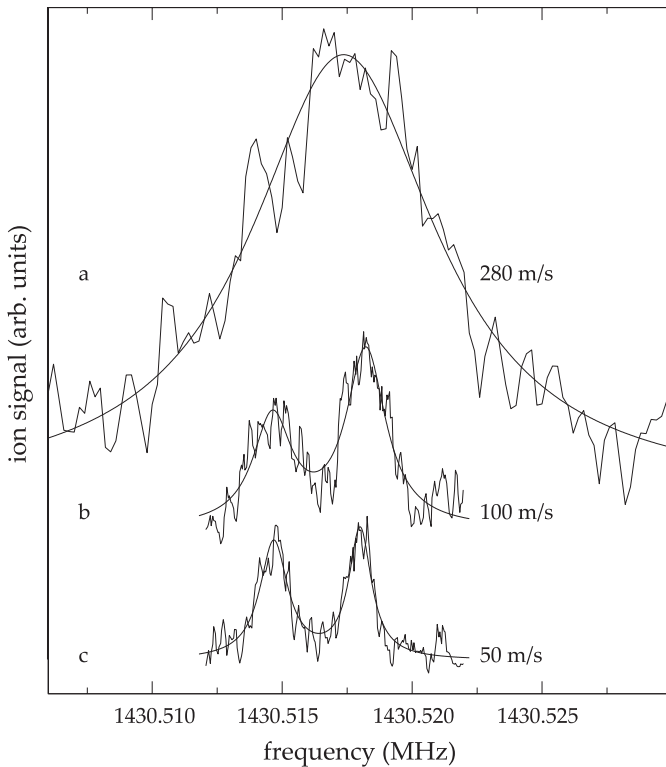


Fig. 3. The $20 \rightarrow 3$ and $21 \rightarrow 2$ transition of $^{15}\text{ND}_3$ recorded in a molecular beam with velocities as indicated. With reduced beam velocities the linewidth decreases from about 10 kHz to about 1 kHz, as determined from fitted Lorentzian line-profiles. The labeling of the lines refers to the numbering of the hyperfine levels as given in Figure 5.

and several distinct features can be observed, a further assignment based on this spectrum alone is not possible. In our previous work [42] we have given a tentative assignment of this spectrum based on scaling the hyperfine interaction parameters deduced for $^{14}\text{ND}_3$. Contrary to the situation in $^{14}\text{ND}_3$, where the quadrupole moment of the ^{14}N nucleus gives rise to readily recognizable splittings in the microwave spectrum, it is not possible to unambiguously identify groups of lines in the microwave spectrum of $^{15}\text{ND}_3$ at this relatively low spectral resolution.

Trace (b) shows the microwave spectrum as measured in a decelerated beam with a mean velocity of 52 m/s, using -20 dBm (2 V/m) of microwave power. It is evident that the spectral resolution of selected individual lines is largely improved relative to the spectrum shown in the upper trace, and many identifiable resonances appear in the spectrum. The strong lines in this spectrum are saturated, however, and, apart from power-broadening, this results in numerous extra lines in the spectrum due to multiple down-up-down Rabi-cycling transitions between hyperfine levels in the upper and lower components of the inversion doublet. This “high power” spectrum of the decelerated beam is therefore mainly useful to identify the weak lines in the inversion spectrum. The central part of the microwave spectrum, which contains the strongest inversion transitions, is measured with a reduced microwave

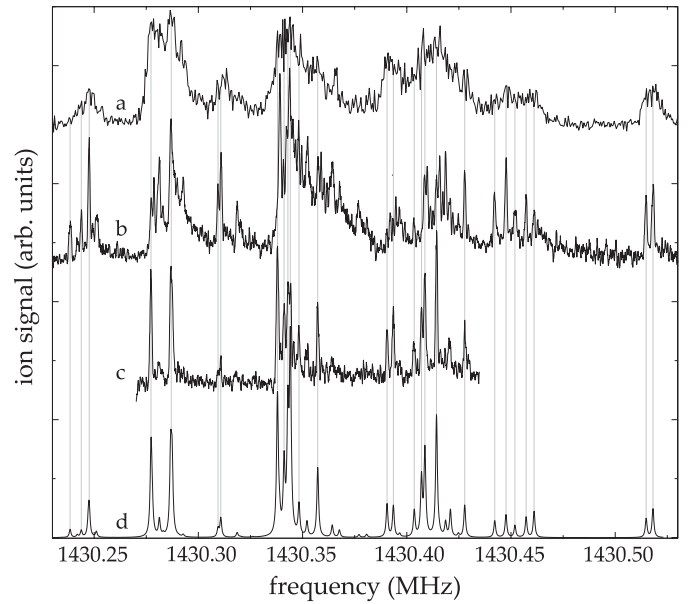


Fig. 4. Microwave inversion spectrum of $^{15}\text{ND}_3$ in the $|J, K\rangle = |1, 1\rangle$ state. Trace (a) shows the spectrum as measured in a beam with a mean velocity of 280 m/s, using -20 dBm (2 V/m in the microwave zone) of microwave power. Trace (b) shows the corresponding measurement for a decelerated beam with a mean velocity of 52 m/s, using -20 dBm (2 V/m) of microwave power. In this spectrum many resonances appear due to multiple down-up-down Rabi-cycling transitions between the upper and lower inversion components. Trace (c) shows the measurement in the decelerated beam at reduced microwave power, -30 dBm (0.6 V/m), under otherwise identical conditions. In trace (d) the theoretically simulated spectrum, convoluted with a Lorentzian lineshape function with a width (FWHM) of 1 kHz, is shown.

power as well. The measured spectrum as recorded, under otherwise identical conditions, with -30 dBm (0.6 V/m) of microwave power is shown in trace (c). In the spectrum several well-resolved strong lines with a linewidth of 1 kHz are observed. The weak lines in the wings of the spectral range shown in trace (b) together with the strong lines shown in trace (c) yield the complete hyperfine resolved microwave inversion spectrum of $^{15}\text{ND}_3$ in the $|J, K\rangle = |1, 1\rangle$ state. In trace (d) the best fitting simulated spectrum, convoluted with a Lorentzian lineshape function with a width (FWHM) of 1 kHz, is shown.

Our simulation of the microwave spectrum covers all the symmetric-top isotopomers of ammonia ($^{14}\text{NH}_3$, $^{15}\text{NH}_3$, $^{14}\text{ND}_3$, $^{15}\text{ND}_3$) [42] through a generalized tensor coupling scheme [51]. This enabled us to test the simulations against the experimentally well characterized $^{14}\text{NH}_3$ system [52]. A detailed description of the formalism that is used is given in the Appendix. For the description of the hyperfine interaction twelve parameters are used. The overall tunneling splitting of the $|J, K\rangle = |1, 1\rangle$ rotational state is given by the parameter c_t . The interaction between the overall rotation and the nuclear spin of ^{15}N is described by the parameters c_{JN1} and c_{JN2} ; there are two parameters since the rotation around the

Table 1. Adjustable parameters in the Hamiltonian, together with their correspondence to parameters in the more commonly used notation from Townes and Schawlow [38]. The values (in kHz) are obtained from the best fit to the experimentally observed transition frequencies. A total of 27 transitions are included in the fit and the overall standard deviation of the fit is 62 Hz. The number in parenthesis is the 1σ standard deviation in the last digit.

parameter	T. & S. [38]	$^{15}\text{ND}_3$ (kHz)
c_t	Ω_t	1430335.66 (2)
$c_{JN1} - c_{JN2}/(2\sqrt{10})$	$-\frac{\sqrt{3}}{2}(a+b)$	8.16 (6)
$c_{JD1} - c_{JD2}/(2\sqrt{10})$	$-\frac{\sqrt{3}}{2}(2A+C)$	4.38 (3)
c_{JD3}	$\sqrt{30}B$	6.45 (10)
c_{ND1}	$-3\sqrt{10}D_1$	-4.74 (27)
c_{ND2}	$\sqrt{30}D_2$	11.62 (15)
c_{DD1}	$3\sqrt{5/2}D_3$	3.40 (22)
c_{DD2}	-	5.08 (11)
c_{QD1}	-	-227.28 (25)
c_{QD2}	-	432.72 (11)

parallel and the perpendicular axes of the symmetric top couple differently to the nuclear spin. The analogous interaction between the overall rotation and the nuclear spin of the deuterium nuclei is described by the parameters c_{JD1} , c_{JD2} , and c_{JD3} ; in this case three parameters are required since the deuterium atoms are located away from the symmetry axis of ammonia. The coupling between the nuclear spin of ^{15}N and the nuclear spin of the deuterium nuclei is described by the parameters c_{ND1} and c_{ND2} and the coupling among the different nuclear spins of deuterium is described by the parameters c_{DD1} and c_{DD2} . Finally, the two parameters c_{QD1} and c_{QD2} describe the interaction between the molecule-fixed electronic wave-function and the laboratory-frame fixed quadrupole moments of the deuterium atoms.

As we have obtained high-resolution microwave spectra for $^{15}\text{ND}_3$ only in a single rovibrational state, the parameters c_{JN1} and c_{JN2} cannot be determined independently; one can only determine a line in c_{JN1} , c_{JN2} space with an a priori known slope, and thus the value of $c_{JN1} - c_{JN2}/(2\sqrt{10})$ is fitted. Different rotational states have different slopes for this line, i.e., different linear combinations can be fitted, from which then the absolute values of the individual parameters c_{JN1} and c_{JN2} can be determined. Similarly, we cannot determine the parameters c_{JD1} and c_{JD2} separately, but their linear combination $c_{JD1} - c_{JD2}/(2\sqrt{10})$ can be extracted from the available data. Therefore, in the fit to the experimental spectrum ten free (combinations of) parameters are adjusted.

The values obtained for these ten parameters from a least-squares fit of the Hamiltonian to the experimental transition frequencies are given in Table 1. In the fit 27 experimental transition frequencies are included and the

Table 2. Experimentally observed and calculated transition frequencies. The labeling of the lines refers to the numbering of the hyperfine levels as given in Figure 5. In the last column the difference Δ between observed and calculated transition frequencies is given.

transition	exp. (kHz)	calc. (kHz)	Δ (kHz)
17→ 11	1430238.50	1430238.46	0.039
18→ 11	1430243.85	1430243.82	0.032
19→ 11	1430247.57	1430247.64	-0.071
16→ 8	1430277.25	1430277.29	-0.039
19→ 9	1430287.06	1430286.99	0.072
17→ 7	1430309.39	1430309.44	-0.046
16→ 6	1430310.77	1430310.77	0.001
21→ 11	1430337.97	1430337.97	-0.005
20→ 10	1430341.16	1430341.13	0.031
17→ 5	1430343.09	1430342.94	0.153
16→ 4	1430344.24	1430344.12	0.123
18→ 5	1430348.25	1430348.29	-0.044
19→ 4	1430357.26	1430357.27	-0.014
14→ 2	1430390.56	1430390.53	0.033
15→ 3	1430393.52	1430393.56	-0.037
22→ 9	1430403.48	1430403.59	-0.108
22→ 8	1430407.07	1430407.05	0.025
20→ 7	1430408.65	1430408.69	-0.037
21→ 6	1430414.30	1430414.26	0.041
19→ 2	1430427.85	1430427.79	0.058
20→ 5	1430442.13	1430442.19	-0.057
21→ 4	1430447.63	1430447.61	0.023
17→ 1	1430451.99	1430451.89	0.096
18→ 1	1430457.27	1430457.25	0.019
19→ 1	1430460.97	1430461.07	-0.104
20→ 3	1430514.80	1430514.83	-0.026
21→ 2	1430518.14	1430518.13	0.014

resulting 1σ standard deviations are given in parenthesis behind the parameter values. Parameters are given with the precision necessary to recalculate the line positions from the given data to within 10% of their standard deviation [53]. The assignment of these 27 transitions together with the experimentally observed and calculated transition frequencies are given in Table 2. In this assignment the labeling of the hyperfine levels as given in Figure 5 is used. The average difference between observed and calculated frequencies is 62 Hz.

The resulting energy-level structure of the inversion doublet of $^{15}\text{ND}_3$ in the $|J, K\rangle = |1, 1\rangle$ state and the Stark curves for these states are shown in Figure 5. Zero energy is chosen at the energy of the lower inversion substate

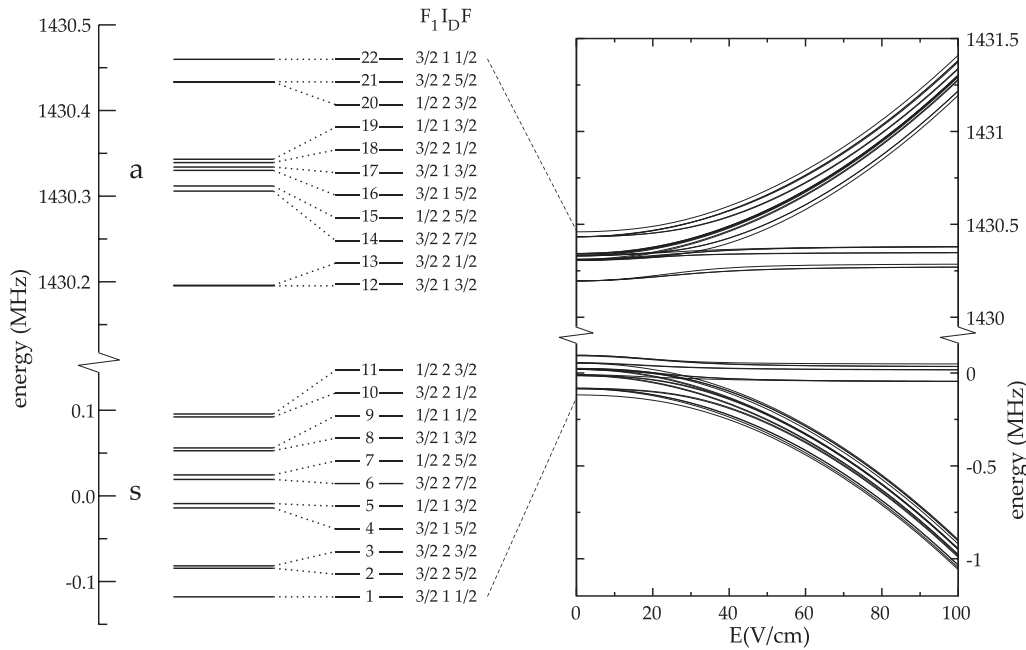


Fig. 5. Labeling and quantum-number assignment of the 22 hyperfine levels in the $|J, K\rangle = |1, 1\rangle$ state of $^{15}\text{ND}_3$. F_1 is the vectorial sum of the overall rotation and the nitrogen nuclear spin, I_D is the angular momentum due to deuterium nuclear spin, and F is the overall angular momentum. On the right-hand side the Stark-shifted hyperfine levels of $^{15}\text{ND}_3$ in the $|J, K\rangle = |1, 1\rangle$ state are shown in electric fields up to 100 V/cm. Note that the scale is broken between the two groups of levels, i.e., that the inversion splitting is not drawn to scale.

with all interactions switched off, i.e., with all parameters in Table 1 except c_t set to zero. In zero electric field both the lower (s) and the upper (a) inversion substate, corresponding to the symmetric and antisymmetric linear combination of the infinite-barrier states, respectively, split up into eleven hyperfine levels, labeled 1–22 with increasing energy. Knowing the interaction parameters for $^{15}\text{ND}_3$ in the $|J, K\rangle = |1, 1\rangle$ state, the behavior of the hyperfine manifold in external fields can be calculated using the same tensor coupling scheme. The dipole moment of $^{15}\text{ND}_3$ is taken as $\mu = 1.48$ D [54]. The energies of all states in zero field are explicitly given in Table 3, together with the number of M_F -components that are high-field seeking in the s-substate and low-field seeking in the a-substate; the remaining states are not affected considerably by the electric field. It is noteworthy that most hyperfine-levels in the upper component of the inversion doublet are exclusively low-field seeking and molecules in these levels can therefore be trapped in field-free regions without potential losses due to Majorana transitions [42].

In the simulated spectrum shown in the lower trace in Figure 4, the relative line intensities are calculated under the assumption that upon entering the microwave zone the population is equally distributed over all the low-field seeking hyperfine levels in the $|J, K\rangle = |1, 1\rangle$ state of $^{15}\text{ND}_3$, and that no population is present in any of the other hyperfine levels. This is substantiated by the experiments, as no transitions from the hyperfine levels 12 and 13, which both hardly shift when an electric field is applied (see Tab. 3), are observed when searching for these

at the predicted microwave frequencies. For the hyperfine levels 14 and 15, of which only some M_F components are high-field seeking, the zero-field population is taken to be equal to the fraction of low-field seeking M_F components, i.e., the population is taken to be 0.25 for level 14 (2 out of 8 M_F components are low-field seeking) and 0.33 for level 15 (2 out of 6 M_F components are low-field seeking). The excellent agreement that is obtained between the observed spectrum and the calculated spectrum, both in line positions and in line intensities, positively demonstrates that there is apparently no further scrambling of the hyperfine levels of the molecules that are focused in the microwave zone. It also demonstrates that there is no observable dependence of the UV-laser based ionization detection scheme on the hyperfine levels of $^{15}\text{ND}_3$, and that the observed relative ion intensities on the various microwave transitions directly reproduce the microwave transition intensities.

3.3 Possible precision measurements on ammonia

Since the inversion mode of ammonia involves tunneling of the hydrogen atoms via a planar configuration to the other side of the nitrogen atom, its frequency is very sensitive to the mass of the proton. This is illustrated by the decrease of the inversion frequency in the $|J, K\rangle = |1, 1\rangle$ level of ammonia from 23.8 GHz to 1.59 GHz or to 0.3 GHz when the hydrogen atoms are replaced by deuterium or by tritium atoms, respectively. Here it should be noted that in

Table 3. Hyperfine energy levels for $^{15}\text{ND}_3$ ($|J, K\rangle = |1, 1\rangle$) as obtained from the best fit to the experimental data; in parentheses the 1σ standard deviation of the relative energy is given. F_1 is the vectorial sum of the overall rotation and the nitrogen nuclear spin, I_D is the angular momentum due to deuterium nuclear spin, and F is the overall angular momentum. For each hyperfine level, the number of M_F components that is shifted — downwards in the s-symmetry level and upwards in the a-symmetry level — is indicated.

s-level						a-level					
label	F_1	I_D	F	energy (kHz)	levels shifted	label	F_1	I_D	F	energy (kHz)	levels shifted
1	3/2	1	1/2	-117.92 (4)	all	12	3/2	1	3/2	1430195.18 (12)	0
2	3/2	2	5/2	-84.64 (3)	all	13	3/2	2	1/2	1430195.80 (12)	0
3	3/2	2	3/2	-81.60 (3)	all	14	3/2	2	7/2	1430305.89 (3)	2
4	3/2	1	5/2	-14.12 (2)	all	15	1/2	2	5/2	1430311.96 (3)	2
5	1/2	1	3/2	-8.96 (3)	all	16	3/2	1	5/2	1430330.00 (3)	all
6	3/2	2	7/2	19.23 (2)	all	17	3/2	1	3/2	1430333.97 (2)	all
7	1/2	2	5/2	24.55 (3)	2	18	3/2	2	1/2	1430339.33 (3)	all
8	3/2	1	3/2	52.71 (4)	0	19	1/2	1	3/2	1430343.15 (3)	all
9	1/2	1	1/2	56.17 (5)	0	20	1/2	2	3/2	1430433.23 (4)	all
10	3/2	2	1/2	92.10 (3)	0	21	3/2	2	5/2	1430433.49 (3)	all
11	1/2	2	3/2	95.51 (3)	0	22	3/2	1	1/2	1430459.76 (6)	all

the Born-Oppenheimer approximation the barrier height is the same for all the isotopomers. The dependence of the tunneling frequency on the proton mass implies that if the proton mass (or rather the ratio of the electron-to-proton mass) varies over time, so does the inversion frequency. Theoretically one expects the inversion frequency, ν_i , to follow the formula

$$\nu_i = \frac{a_0}{\sqrt{\mu}} e^{a_1 \sqrt{\mu}}$$

with μ the reduced mass of ammonia and a_0 and a_1 constants [38, 55]. From the known frequencies for the inversion mode of the ammonia isotopomers [42, 52, 55] we find $a_0 = 68 \text{ GHz} \times u^{1/2}$ and $a_1 = 4.7 u^{-1/2}$. From this, we can determine the sensitivity of the inversion frequency to changes in the electron-to-proton mass ratio m_e/m_p . When m_e/m_p changes by $\Delta(m_e/m_p)$ and the neutron mass changes by the same amount as the proton mass [56], the reduced mass changes by $\mu \Delta(m_e/m_p)$ and the inversion frequency in $^{15}\text{ND}_3$ changes as

$$\frac{\Delta \nu_i}{\nu_i} = -5.6 \frac{\Delta(m_e/m_p)}{m_e/m_p}.$$

By comparing the inversion frequency with a suitable frequency standard, for instance the cesium clock, over an extended period of time, the time variation of m_e/m_p , or an upper limit thereof, can be determined. In order to be able to detect a variation at the level of 3×10^{-15} /year, the bound obtained from astrophysical data [16], the present accuracy needs to be improved by a factor of 10^6 . It is

conceivable that this resolution can be achieved if a molecular fountain, in which interaction times of seconds can be reached, is constructed.

4 Conclusions

In this work we have demonstrated the use of a decelerated and transversally and longitudinally focused molecular beam in high-resolution spectroscopy. In a pulsed beam of $^{15}\text{ND}_3$, decelerated to 52 m/s, the hyperfine structure on the inversion doubling transition in the $|J, K\rangle = |1, 1\rangle$ state around 1.43 GHz is completely resolved. The transit-time limited linewidths in the microwave-UV double resonance experiments are about 1 kHz, and the standard deviation from the best-fitting simulated spectrum is 62 Hz. All 22 individual hyperfine levels of $^{15}\text{ND}_3$ in the $|J, K\rangle = |1, 1\rangle$ state are assigned and their absolute energies are determined to an accuracy of better than 100 Hz. Our experimental approach is generally applicable to high-resolution spectroscopy of polar molecules, and the obtainable spectral resolution can still be readily improved if longer interaction zones and/or slower molecular beams, in particular molecular fountains, would be employed.

This work is part of the research program of the *Stichting voor Fundamenteel Onderzoek der Materie (FOM)*, which is financially supported by the *Nederlandse Organisatie voor Wetenschappelijk Onderzoek (NWO)*. We acknowledge the help of Rienk T. Jongma in the initial stages of this experiment and the advice of Waldo Bongers and Marc van der Pol on

microwave technology, as well as the discussions with Wim Ubachs on experiments testing time-variation of fundamental constants.

Appendix: Tensor treatment of the Hamiltonian

Three types of hyperfine interaction are relevant for the ammonia molecule.

1. The interaction of the nuclear quadrupole moments with the inhomogeneous intramolecular electrostatic field. For the n th nucleus one can write the interaction term as

$$V_q = \frac{1}{6} \sum_{i,j} Q_{i,j}^{(n)} \frac{\partial^2 \varphi(\mathbf{R}^{(n)})}{\partial x_i \partial x_j}$$

where $Q_{i,j}^{(n)}$ are the Cartesian components of the quadrupole moment of the n th nucleus, φ is the intramolecular electrostatic potential, and $\mathbf{R}^{(n)}$ is the radius-vector of the n th nucleus with x_i being its Cartesian components.

2. The interaction of the magnetic moments of the nuclei with the intramolecular magnetic field induced by the rotational motion of the molecule. For a given particle n the interaction term reads

$$V_m = -\boldsymbol{\mu}^{(n)} \cdot \mathbf{H}(\mathbf{R}^{(n)})$$

where $\boldsymbol{\mu}^{(n)}$ and $\mathbf{R}^{(n)}$ are the magnetic moment and radius-vector of the n th particle, respectively. The strength of the magnetic field acting on the n th particle, arising from the rotational motion of the molecule, can be phenomenologically described as a linear function of the angular momentum of the molecule:

$$\mathbf{H}(\mathbf{R}^{(n)}) = \hat{L}(\mathbf{R}^{(n)}) \mathbf{J}.$$

3. The interaction between the magnetic moments of different nuclei. The magnetic moment of a particle is defined via its spin as [57]:

$$\boldsymbol{\mu} = \mu(\hat{s}/S)$$

where μ is the value of the magnetic moment, \hat{s} is the spin operator of the particle, and S is the absolute value of the spin. The interaction term, which is referred to as the spin-spin interaction term, is:

$$V_{SS} = \frac{R_{nm}^2 \boldsymbol{\mu}^{(n)} \cdot \boldsymbol{\mu}^{(m)} - 3(\boldsymbol{\mu}^{(n)} \cdot \mathbf{R}_{nm})(\boldsymbol{\mu}^{(m)} \cdot \mathbf{R}_{nm})}{R_{nm}^5}$$

with \mathbf{R}_{nm} the radius-vector between the n th and m th particle, and with $\boldsymbol{\mu}^{(n)}$ and $\boldsymbol{\mu}^{(m)}$ the magnetic moments of the n th and m th particles, respectively.

The latter two types of hyperfine interaction are also applicable for electrons. As the electronic shell is closed in

the electronic ground state of ammonia, neither the spin-orbit nor the spin-spin electronic interactions contribute to its hyperfine splitting of the tunneling-rotation-vibration states, however.

In this work the point symmetry group formalism is applied to calculate the hyperfine splitting of the $|J, K\rangle = |1, 1\rangle$ vibrational ground state of $^{15}\text{ND}_3$. The usefulness of the application of Racah algebra to molecular point symmetry groups is well documented for the case of the hyperfine splitting problem [51]. For the calculation of rotation-vibration spectra of spherical top molecules the molecular point symmetry group formalism has been elaborated as well [58].

Here we follow the molecular point symmetry group formalism conventions used in reference [59]. The basic operators that appear in the hyperfine Hamiltonian are treated as double tensors $\hat{T}^{(R,\Gamma)}$. The index R designates the angular momentum rank of the tensor \hat{T} with respect to the O_3 rotation symmetry group in the laboratory coordinate system. The index Γ designates the irreducible representation of the molecular point symmetry group, which describes the symmetry properties of the tensor in the framework of the molecular coordinate system. The complete point symmetry group of ammonia is D_{3h} , but to simplify the notation here the subgroup D_3 nomenclature is used, thus omitting *gerade/ungerade* indices. The operators relevant for the hyperfine structure problem of ammonia are:

- the spin operator $\hat{S}_N^{(1,A_1)}$ of the nitrogen nucleus;
- the deuterium nuclear spin operators reduced to irreducible representations (irreps) as

$$\hat{S}_D^{(1,A_1)} = \frac{1}{\sqrt{3}} \left(\hat{S}_D(1) + \hat{S}_D(2) + \hat{S}_D(3) \right)$$

$$\hat{S}_{D,x}^{(1,E)} = \frac{1}{\sqrt{6}} \left(2\hat{S}_D(1) - \hat{S}_D(2) - \hat{S}_D(3) \right)$$

$$\hat{S}_{D,y}^{(1,E)} = \frac{1}{\sqrt{2}} \left(\hat{S}_D(2) - \hat{S}_D(3) \right)$$

where $\hat{S}_D(n)$ is the spin operator of the n th nucleus and A_1 and E designate the molecular symmetry group components. The molecule-fixed coordinate system, with its origin in the center of mass, is oriented with the z -axis pointing towards the nitrogen nucleus, and with the deuterium nucleus numbered 1 in the xz -plane;

- the angular momentum operator $\hat{J}_M^{(1,A_1)}$ with the projection M on the laboratory system of coordinates;
- the Wigner function of rank R which describes the orientation of the molecular tensors with respect to the laboratory system of coordinates, $D_{M,\sigma}^{(R,\Gamma)}(\alpha, \beta, \gamma)$. Here α , β , and γ are the Euler angles describing the orientation of the molecule-fixed system of coordinates relative to the laboratory-fixed system of coordinates, M designates the projection on the laboratory Z -axis, Γ and σ designate the point symmetry group

irreducible representation and its component in the framework of molecular point symmetry group, respectively. In the calculations three symmetry adopted Wigner functions are used, $D^{(2A_1)}$ and $D^{(2E)}_{(\kappa=2)}$, which appear in the hyperfine Hamiltonian, and $D^{(1A_2)}$, which appears in the formula for the dipole moment matrix elements between tunneling levels. The explicit formulas for these functions are

$$\begin{aligned} D_M^{(2A_1)} &= D_{M,K=0}^{(2)*} \\ D_{(\kappa=2)M,x}^{(2E)} &= \left(D_{M,K=-2}^{(2)*} - D_{M,K=2}^{(2)*} \right) / \sqrt{2} \\ D_{(\kappa=2)M,y}^{(2E)} &= i \left(D_{M,K=-2}^{(2)*} + D_{M,K=2}^{(2)*} \right) / \sqrt{2} \\ D^{(1A_2)} &= D_{M,K=0}^{(1)*}. \end{aligned}$$

The higher order spin operators relevant for the hyperfine problem are derived using the following relationships:

$$\begin{aligned} \hat{S}_N^{(2,A_1)} &= \left(\hat{S}_N^{(1,A_1)} \otimes \hat{S}_N^{(1,A_1)} \right)^{(2,A_1)} \\ \hat{S}_D^{(2,A_1)} &= \frac{1}{\sqrt{3}} \left(\left(\hat{S}(2) \otimes \hat{S}(3) \right)^{(2)} + \left(\hat{S}(3) \otimes \hat{S}(1) \right)^{(2)} \right. \\ &\quad \left. + \left(\hat{S}(1) \otimes \hat{S}(2) \right)^{(2)} \right) \\ \hat{S}_{D,x}^{(2,E)} &= \frac{1}{\sqrt{6}} \left(2 \left(\hat{S}(2) \otimes \hat{S}(3) \right)^{(2)} - \left(\hat{S}(3) \otimes \hat{S}(1) \right)^{(2)} \right. \\ &\quad \left. - \left(\hat{S}(1) \otimes \hat{S}(2) \right)^{(2)} \right) \\ \hat{S}_{D,y}^{(2,E)} &= \frac{1}{\sqrt{2}} \left(\left(\hat{S}(3) \otimes \hat{S}(1) \right)^{(2)} - \left(\hat{S}(1) \otimes \hat{S}(2) \right)^{(2)} \right) \\ \hat{S}_{Dq}^{(2,A_1)} &= \frac{1}{\sqrt{3}} \left(\left(\hat{S}(1) \otimes \hat{S}(1) \right)^{(2)} + \left(\hat{S}(2) \otimes \hat{S}(2) \right)^{(2)} \right. \\ &\quad \left. + \left(\hat{S}(3) \otimes \hat{S}(3) \right)^{(2)} \right) \\ \hat{S}_{Dq,x}^{(2,E)} &= \frac{1}{\sqrt{6}} \left(2 \left(\hat{S}(1) \otimes \hat{S}(1) \right)^{(2)} - \left(\hat{S}(2) \otimes \hat{S}(2) \right)^{(2)} \right. \\ &\quad \left. - \left(\hat{S}(3) \otimes \hat{S}(3) \right)^{(2)} \right) \\ \hat{S}_{Dq,y}^{(2,E)} &= \frac{1}{\sqrt{2}} \left(\left(\hat{S}(2) \otimes \hat{S}(2) \right)^{(2)} - \left(\hat{S}(3) \otimes \hat{S}(3) \right)^{(2)} \right). \end{aligned}$$

Herein the tensor coupling for the laboratory projections of the spin operators is defined according to the well-known relationship

$$(S(a) \otimes S(b))_m^{(2)} = \sum_{m_1, m_2} C_{1m_1, 1, m_2}^2 S(a)_{m_1} S(b)_{m_2}$$

with the Clebsch-Gordon coefficient $C_{1m_1, 1, m_2}^2$. The coupling of two double tensors A and B , yielding the tensor of

rank R and symmetry Γ , in the framework of the molecular symmetry group formalism is

$$\begin{aligned} \left(A^{(R_1\Gamma_1)} \otimes B^{(R_2\Gamma_2)} \right)_{\mu\sigma}^{(R\Gamma)} = \\ \sum_{\mu_1, \mu_2, \sigma_1, \sigma_2} C_{R_1\mu_1, R_2\mu_2}^{R\mu} C_{\Gamma_1\sigma_1, \Gamma_2\sigma_2}^{\Gamma\sigma} \cdot A_{\mu_1\sigma_1}^{(R_1\Gamma_1)} \cdot B_{\mu_2\sigma_2}^{(R_2\Gamma_2)} \quad (\text{A.1}) \end{aligned}$$

where $C_{R_1\mu_1, R_2\mu_2}^{R\mu}$ is the Clebsch-Gordon coefficient in the $O(3)$ group and $C_{\Gamma_1\sigma_1, \Gamma_2\sigma_2}^{\Gamma\sigma}$ is the Clebsch-Gordon coefficient in the D_3 symmetry group [51].

The hyperfine Hamiltonian for a certain rotation-vibration level of ammonia [38, 60] can be rewritten using the above coupling relationship:

$$\begin{aligned} H = c_t \times O_t^{(0A_1)} \\ + c_{QN} \times \left(D^{(2A_1)} \otimes \hat{S}_N^{(2,A_1)} \right)^{(0A_1)} \\ + \delta c_{QN} \times O_t^{(0A_1)} \cdot \left(D^{(2A_1)} \otimes \hat{S}_N^{(2,A_1)} \right)^{(0A_1)} \\ + c_{JN1} \times \left(J^{(1A_1)} \otimes S_N^{(1A_1)} \right)^{(0A_1)} \\ + c_{JN2} \times \left(\left(D^{(2A_1)} \otimes J^{(1A_1)} \right)^{(1A_1)} \otimes S_N^{(1A_1)} \right)^{(0A_1)} \\ + c_{JD1} \times \left(J^{(1A_1)} \otimes S_D^{(1A_1)} \right)^{(0A_1)} \\ + c_{JD2} \times \left(\left(D^{(2A_1)} \otimes J^{(1A_1)} \right)^{(1A_1)} \otimes S_D^{(1A_1)} \right)^{(0A_1)} \\ + c_{JD3} \times \left(\left(D_{(\kappa=2)}^{(2E)} \otimes J^{(1A_1)} \right)^{(1E)} \otimes S_D^{(1E)} \right)^{(0A_1)} \\ + c_{ND1} \times \left(\left(D^{(2A_1)} \otimes S_N^{(1A_1)} \right)^{(1A_1)} \otimes S_D^{(1A_1)} \right)^{(0A_1)} \\ + c_{ND2} \times \left(\left(D_{(\kappa=2)}^{(2E)} \otimes S_N^{(1A_1)} \right)^{(1E)} \otimes S_D^{(1E)} \right)^{(0A_1)} \\ + c_{DD1} \times \left(D^{(2A_1)} \otimes \hat{S}_D^{(2A_1)} \right)^{(0A_1)} \\ + c_{DD2} \times \left(D_{(\kappa=2)}^{(2E)} \otimes \hat{S}_D^{(2E)} \right)^{(0A_1)} \\ + c_{QD1} \times \left(D^{(2A_1)} \otimes \hat{S}_{Dq}^{(2A_1)} \right)^{(0A_1)} \\ + c_{QD2} \times \left(D_{(\kappa=2)}^{(2E)} \otimes \hat{S}_{Dq}^{(2E)} \right)^{(0A_1)} \end{aligned}$$

with the tunneling operator $O_t^{(0A_1)}$, which is defined in the two dimensional space of $|s\rangle$ symmetric and $|a\rangle$ antisymmetric tunneling states. Its only non-zero matrix element is $\langle a | O_t | a \rangle = 1$. The parameter c_t is the effective tunneling splitting of the rotation-vibration level, the parameters c_{QN} and δc_{QN} are the quadrupole interaction parameters of the nitrogen nucleus and its difference in the symmetric and antisymmetric tunneling levels, respectively.

The two c_{JNi} parameters describe the magnetic interaction of the nitrogen nuclear spin with the overall rotation of the molecule, the three c_{JD_i} parameters describe the magnetic interaction of the deuterium nuclear spin with the overall rotation of the molecule, the two parameters c_{ND_i} describe the spin-spin interaction between the nitrogen and the deuterium nuclei, the two parameters c_{DD_i} describe the spin-spin interaction between the different deuterium nuclei, and the last two parameters c_{QD_i} are the quadrupole interaction parameter of the deuterium nuclei. The product of generally non-commuting operators $(D^{(R_1\Gamma_1)} \otimes J^{(R_2\Gamma_2)})^{(R\Gamma)}$ in the above formula is the symmetrized form

$$\frac{1}{2} \left[\left(D^{(R_1\Gamma_1)} \otimes J^{(R_2\Gamma_2)} \right)^{(R\Gamma)} + \left(J^{(R_2\Gamma_2)} \otimes D^{(R_1\Gamma_1)} \right)^{(R\Gamma)} \right].$$

The wavefunctions relevant for the $|J, K\rangle = |1, 1\rangle$ state of ammonia include the tunneling wavefunction $\psi_t^{(0\Gamma_t)}$ of rank 0 and symmetry Γ_t (A_1 symmetry for the symmetric tunneling state and A_2 symmetry for the antisymmetric tunneling state), the rotational wave function $\psi_r^{(JE)}$ of the $|J, K\rangle = |1, 1\rangle$ state adopted to the E irrep of the D_3 point symmetry group [51], the spin wavefunction $\psi_N^{(S_N A_1)}$ of the nitrogen nucleus, and the spin wavefunctions $\psi_D^{(S_D \Gamma_D)}$ of the deuterium nuclei. A classification of possible S_D quantum numbers and of Γ_D symmetry species relevant for a given J, K rotational state can be found elsewhere [51].

The basic set of wavefunction was built up in the framework of the tensor coupling formalism, i.e., using the relationship for coupling of tensors as given in equation (A.1):

$$\begin{aligned} & \left(\left(\left(\psi_t^{(0\Gamma_t)} \otimes \psi_r^{(JE)} \right)^{(J\Gamma_{tr})} \otimes \psi_N^{(S_N A_1)} \right)^{(F_1\Gamma_1)} \right. \\ & \left. \otimes \psi_D^{(S_D \Gamma_D)} \right)_{M_F \Sigma}^{(F\Gamma)} \end{aligned}$$

where $J, \Gamma_{tr}, F_1, \Gamma_1$ are the intermediate quantum numbers. F_1 is known to be an approximately good quantum number in the case of $^{14}\text{ND}_3$, as a result of the large quadrupole interaction parameter of the ^{14}N nucleus, but this is not the case for $^{15}\text{ND}_3$. F is the total angular momentum, Γ is the overall symmetry of the hyperfine wavefunction, and M_F and Σ are the projection quantum number of the overall angular momentum F and the projection index of the Γ irrep, respectively.

The tensor coupling formalism allows to use a straightforward procedure for the calculation of the matrix elements of operators. First, the Wigner-Eckart theorem for the operator $O_{\mu s}^{(R\Gamma)}$ in the framework of the symmetry

group formalism is used:

$$\begin{aligned} & \langle j\gamma' m' \sigma' | O_{\mu s}^{(R\Gamma)} | j\gamma m \sigma \rangle = \\ & (-1)^{j'-m'} \begin{pmatrix} j' & R & j \\ -m' & \mu & m \end{pmatrix} \begin{pmatrix} \gamma' & \Gamma & \gamma \\ \sigma' & s & \sigma \end{pmatrix} \langle j'\gamma' || O^{(R\Gamma)} || j\gamma \rangle. \end{aligned} \quad (\text{A.2})$$

Here $|j\gamma m \sigma\rangle$ designates a wavefunction which is a tensor of rank j and symmetry γ with m and σ being the appropriate projection indices, $\langle j'\gamma' || O^{(R\Gamma)} || j\gamma \rangle$ is the reduced matrix element, $\begin{pmatrix} j' & R & j \\ -m' & \mu & m \end{pmatrix}$ is the $3J$ -symbol of the $O(3)$ group and $\begin{pmatrix} \gamma' & \Gamma & \gamma \\ \sigma' & s & \sigma \end{pmatrix}$ is the 3Γ -symbol of the molecular symmetry group. For explicit formulas of the 3Γ -symbols of the D_3 group the reader is referred to Cederberg [51].

Second, in the basis of the coupled wavefunctions the general formula for the reduced matrix element of the coupled operator is given as

$$\begin{aligned} & \langle (j'_1 \gamma'_1 j'_2 \gamma'_2) j' \gamma' || \left(A^{(R_1\Gamma_1)} \otimes B^{(R_2\Gamma_2)} \right)^{(R\Gamma)} || (j_1 \gamma_1 j_2 \gamma_2) j \gamma \rangle \\ & = \Pi_{j'} \Pi_R \Pi_j \begin{Bmatrix} R_1 & R_2 & R \\ j'_1 & j'_2 & j' \\ j_1 & j_2 & j \end{Bmatrix} \Pi_{\gamma'} \Pi_\Gamma \Pi_\gamma \begin{Bmatrix} \Gamma_1 & \Gamma_2 & \Gamma \\ \gamma'_1 & \gamma'_2 & \gamma' \\ \gamma_1 & \gamma_2 & \gamma \end{Bmatrix} \\ & \times \langle j'_1 \gamma'_1 || A^{(R_1\Gamma_1)} || j_1 \gamma_1 \rangle \langle j'_2 \gamma'_2 || B^{(R_2\Gamma_2)} || j_2 \gamma_2 \rangle \quad (\text{A.3}) \end{aligned}$$

with the square root Π_γ of the dimension of space γ , i.e., $\Pi_J = \sqrt{2J+1}$, $\Pi_A = \sqrt{1}$, and $\Pi_E = \sqrt{2}$.

Explicit formulas for the $9J$ -symbols

$$\begin{Bmatrix} R_1 & R_2 & R \\ j'_1 & j'_2 & j' \\ j_1 & j_2 & j \end{Bmatrix}$$

and for the 9Γ -symbols

$$\begin{Bmatrix} \Gamma_1 & \Gamma_2 & \Gamma \\ \gamma'_1 & \gamma'_2 & \gamma' \\ \gamma_1 & \gamma_2 & \gamma \end{Bmatrix}$$

are presented in [51, 61–63]. By recursively applying the equations (A.2) and (A.3) all relevant matrix elements can be evaluated, as the reduced matrix elements of fundamental operators are well-known [51].

References

1. M. Niering, R. Holzwarth, J. Reichert, P. Pokasov, T. Udem, M. Weitz, T.W. Hänsch, P. Lemonde, G. Santarelli, M. Abgrall, P. Laurent, C. Salomon, A. Clairon, Phys. Rev. Lett. **84**, 5496 (2000)
2. T. Udem, A. Huber, B. Gross, J. Reichert, M. Prevedelli, M. Weitz, T.W. Hänsch, Phys. Rev. Lett. **79**, 2646 (1997)

3. B. de Beauvoir, F. Nez, L. Julien, B. Cagnac, F. Biraben, D. Touahri, L. Hilico, O. Acef, A. Clairon, J.J. Zondy, *Phys. Rev. Lett.* **78**, 440 (1997)
4. C. Schwob, L. Jozefowski, B. de Beauvoir, L. Hilico, E. Nez, L. Julien, F. Biraben, O. Acef, J.J. Zondy, A. Clairon, *Phys. Rev. Lett.* **86**, 4193 (2001)
5. E. Arimondo, P. Glorieux, T. Oka, *Opt. Comm.* **23**, 369 (1977)
6. J. Crassous, F. Monier, J.P. Dutasta, M. Ziskind, C. Daussy, C. Grain, C. Chardonnet, *Chem. Phys. Chem.* **4**, 541 (2003)
7. M. Quack, *Angew. Chem. Int. Ed.* **41**, 4618 (2002)
8. W.A. Bonner, *Chirality* **12**, 114 (2000)
9. M. Ziskind, C. Daussy, T. Marrel, C. Chardonnet, *Eur. Phys. J. D* **20**, 219 (2002)
10. S.G. Karshenboim, *Can. J. Phys.* **78**, 639 (2000)
11. J.P. Uzan, *Rev. Mod. Phys.* **75**, 403 (2003)
12. J.K. Webb, M.T. Murphy, V.V. Flambaum, V.A. Dzuba, J.D. Barrow, C.W. Churchill, J.X. Prochaska, A.M. Wolfe, *Phys. Rev. Lett.* **87**, 091301 (2001)
13. L.L. Cowie, A. Songaila, *Nature* **428**, 132 (2004)
14. R. Srianand, H. Chand, P. Petitjean, B. Aracil, *Phys. Rev. Lett.* **92**, 121302 (2004)
15. R.I. Thompson, *Astrophys. Lett. Comm.* **16**, 3 (1975)
16. W. Ubachs, E. Reinhold, *Phys. Rev. Lett.* **92**, 101302 (2004)
17. J.J. Hudson, B.E. Sauer, M.R. Tarbutt, E.A. Hinds, *Phys. Rev. Lett.* **89**, 023003 (2002)
18. D. Kawall, F. Bay, S. Bickman, Y. Jiang, D. DeMille, *Phys. Rev. Lett.* **92**, 173007 (2004)
19. D. DeMille, *Bull. Am. Phys. Soc.* **49**, 97 (2004)
20. N.F. Ramsey, *Rev. Mod. Phys.* **62**, 541 (1990)
21. H. Katori, M. Takamoto, V.G. Pal'chikov, V.D. Ovsiannikov, *Phys. Rev. Lett.* **91**, 173005 (2003)
22. M.A. Kasevich, E. Riis, S. Chu, R.G. Devoe, *Phys. Rev. Lett.* **63**, 612 (1989)
23. C. Audoin, B. Guinot, *The Measurement of Time* (Cambridge University Press, 2001)
24. P.E. Durand, G. Nogues, V. Bernard, A. AmyKlein, C. Chardonnet, *Europhys. Lett.* **37**, 103 (1997)
25. A. Amy-Klein, L.F. Constantin, R.J. Butcher, C. Daussy, P.E. Durand, G. Nogues, C. Chardonnet, *Opt. Exp.* **4**, 67 (1999)
26. H.L. Bethlem, G. Meijer, *Int. Rev. Phys. Chem.* **22**, 73 (2003)
27. M.R. Tarbutt, H.L. Bethlem, J.J. Hudson, V.L. Ryabov, V.A. Ryzhov, B.E. Sauer, G. Meijer, E.A. Hinds, *Phys. Rev. Lett.* **92**, 173002 (2004)
28. F. Masnou-Seeuws, P. Pillet, *Adv. At. Mol. Opt. Phys.* **47**, 53 (2001)
29. C.A. Regal, C. Ticknor, J.L. Bohn, D.S. Jin, *Nature* **424**, 47 (2003)
30. R. deCarvalho, J.M. Doyle, B. Friedrich, T. Guillet, J. Kim, D. Patterson, J.D. Weinstein, *Eur. Phys. J. D* **7**, 289 (1999)
31. J.D. Weinstein, R. deCarvalho, T. Guillet, B. Friedrich, J.M. Doyle, *Nature* **395**, 148 (1998)
32. D. Egorov, J.D. Weinstein, D. Patterson, B. Friedrich, J.M. Doyle, *Phys. Rev. A* **63**, 030501 (2001)
33. S.A. Rangwala, T. Junglen, T. Rieger, P.W.H. Pinkse, G. Rempe, *Phys. Rev. A* **67**, 043406 (2003)
34. M. Gupta, D. Herschbach, *J. Phys. Chem. A* **103**, 10670 (1999)
35. M. Gupta, D. Herschbach, *J. Phys. Chem. A* **105**, 1626 (2001)
36. M.S. Elioff, J.J. Valentini, D.W. Chandler, *Science* **302**, 1940 (2003)
37. C.E. Cleeton, N.H. Williams, *Phys. Rev.* **45**, 234 (1934)
38. C.H. Townes, A.L. Schawlow, *Microwave Spectroscopy* (Dover Publications, New York, 1975)
39. S.G. Kukolich, *Phys. Rev.* **138**, 1322 (1965)
40. L. Fusina, M. Carlotti, G. Dilonardo, S.N. Murzin, O.N. Stepanov, *J. Mol. Spec.* **147**, 71 (1991)
41. S.N. Murzin, B.D. Osipov, *Opt. Spectrosc. (USSR)* **53**, 579 (1982)
42. J. van Veldhoven, R.T. Jongma, B. Sartakov, W.A. Bongers, G. Meijer, *Phys. Rev. A* **66**, 032501 (2002)
43. F.M.H. Cromptvoets, R.T. Jongma, H.L. Bethlem, A.J.A. van Roij, G. Meijer, *Phys. Rev. Lett.* **89**, 093004 (2002)
44. J.P. Gordon, H.J. Zeiger, C.H. Townes, *Phys. Rev.* **95**, 282 (1954)
45. J.P. Gordon, H.J. Zeiger, C.H. Townes, *Phys. Rev.* **99**, 1264 (1955)
46. H.L. Bethlem, G. Berden, G. Meijer, *Phys. Rev. Lett.* **83**, 1558 (1999)
47. H.L. Bethlem, G. Berden, A.J.A. van Roij, F.M.H. Cromptvoets, G. Meijer, *Phys. Rev. Lett.* **84**, 5744 (2000)
48. H.L. Bethlem, F.M.H. Cromptvoets, R.T. Jongma, S.Y.T. van de Meerakker, G. Meijer, *Phys. Rev. A* **65**, 053416 (2002)
49. M.N.R. Ashfold, R.N. Dixon, N. Little, R.J. Stickland, C.M. Western, *J. Chem. Phys.* **89**, 1754 (1988)
50. W. Demtröder, *Laser Spectroscopy: Basic Concepts and Instrumentation*, 3rd edn. (Springer Verlag, Berlin, 2003)
51. J.W. Cederberg, *Am. J. Phys.* **40**, 159 (1972)
52. S.G. Kukolich, *Phys. Rev.* **156**, 83 (1967)
53. J.K.G. Watson, *J. Mol. Spec.* **66**, 500 (1977)
54. R.L. Bhattacharjee, L.H. Johnson, R.D. Sudhakaran, J.C. Sarker, *J. Mol. Spec.* **138**, 38 (1989)
55. P. Helminger, F.C.D. Lucia, W. Gordy, H.W. Morgan, P.A. Staats, *Phys. Rev. A* **9**, 12 (1974)
56. V.V. Flambaum, D.B. Leinweber, A.W. Thomas, R.D. Young, *Phys. Rev. D* **69**, 115006 (2004); V.V. Flambaum, private communication
57. L.D. Landau, E.M. Lifshitz, *Quantum Mechanics*, volume 3 of *Course of Theoretical Physics*, 3rd edn. (Butterworth Heinemann, Oxford, 2000)
58. J.P. Champion, M. Loete, G. Pierre, In *Spectroscopy of the Earth's atmosphere and interstellar medium*, edited by N. Rao, A. Weber (Academic Press, Columbus, OH, USA, 1992), pages 339–422
59. B.G. Sartakov, J. Oomens, J. Reuss, A. Fayt, *J. Mol. Spec.* **185**, 31 (1997)
60. R.L. Cook, F.C. de Lucia, *Am. J. Phys.* **39**, 1433 (1971)
61. A.R. Edmonds, *Angular momentum in quantum mechanics* (Princeton University Press, Princeton, NJ, USA, 1957)
62. B.R. Judd, *Angular momentum theory for diatomic molecules* (Academic Press, New York, NY, USA, 1975)
63. R.N. Zare, *Angular momentum* (John Wiley & Sons, New York, NY, USA, 1987)